Spectral analysis of nonlinear flows

CLARENCE W. ROWLEY[1]†, IGOR MEZIĆ[2], SHERVIN BAGHERI[3], PHILIPP SCHLATTER[3] AND DAN S. HENNINGSON[3]

[1]Department of Mechanical and Aerospace Engineering, Princeton University, NJ 08544, USA

[2]Department of Mechanical Engineering, University of California, Santa Barbara, CA 93106-5070, USA

[3]Linné Flow Centre, Department of Mechanics, Royal Institute of Technology (KTH), SE-10044 Stockholm, Sweden

We present a technique for describing the global behaviour of complex nonlinear flows by decomposing the flow into modes determined from spectral analysis of the Koopman operator, an infinite-dimensional linear operator associated with the full nonlinear system. These modes, referred to as Koopman modes, are associated with a particular observable, and may be determined directly from data (either numerical or experimental) using a variant of a standard Arnoldi method. They have an associated temporal frequency and growth rate and may be viewed as a nonlinear generalization of global eigenmodes of a linearized system. They provide an alternative to proper orthogonal decomposition, and in the case of periodic data the Koopman modes reduce to a discrete temporal Fourier transform. The Arnoldi method used for computations is identical to the dynamic mode decomposition recently proposed by Schmid & Sesterhenn (*Sixty-First Annual Meeting of the APS Division of Fluid Dynamics*, 2008), so dynamic mode decomposition can be thought of as an algorithm for finding Koopman modes. We illustrate the method on an example of a jet in crossflow, and show that the method captures the dominant frequencies and elucidates the associated spatial structures.

1. Introduction

Many fluid flows exhibit complex phenomena that occur on a wide range of scales in both space and time. Even with large amounts of information available from simulations, and comprehensive experimental measurements such as time-resolved particle image velocimetry (PIV), analysis of complex flow phenomena directly from raw time histories of the dynamics is usually not fruitful. In practice, one often analyses flow structures by decomposing them into *modes*. Common techniques include global eigenmodes for linearized dynamics (see e.g. Bagheri *et al.* 2009*b*), discrete Fourier transforms, proper orthogonal decomposition (POD) for nonlinear flows (Holmes, Lumley & Berkooz 1996), balancing modes for linear systems (Rowley 2005) and many variants of these techniques, such as using shift modes (Noack *et al.* 2003) in conjunction with POD modes.

Here, we present a modal decomposition for nonlinear flows based on spectral analysis of a linear operator, called the *Koopman operator*, that is defined for any

---

† Email address for correspondence: cwrowley@princeton.edu

nonlinear system. Even if the governing dynamics are finite dimensional, the Koopman operator is infinite dimensional, and does not rely on linearization of the dynamics: indeed, it captures the full information of the nonlinear system. This operator has been used to analyse nonlinear dynamical systems, for instance in Mezić & Banaszuk (2004) and Mezić (2005), and in these works it was shown that for nonlinear systems evolving on an attractor, modes corresponding to eigenvalues of the Koopman operator may be computed using *harmonic averages* or discrete Fourier transforms.

The paper is organized as follows. In §2, we define the Koopman operator and its modes associated with a particular observable. In §3, we show that one may compute approximations to these eigenvalues and their associated modes using a version of the familiar Arnoldi algorithm that does not require knowledge of an underlying linear operator. This algorithm is the same as that referred to as dynamic mode decomposition by Schmid & Sesterhenn (2008). Finally, in §4, we illustrate the method on an example of a jet in crossflow.

2. Koopman operator and Koopman modes

Consider a dynamical system evolving on a manifold M such that, for $\boldsymbol{x}_k \in M$,

$$\boldsymbol{x}_{k+1} = \boldsymbol{f}(\boldsymbol{x}_k), \tag{2.1}$$

where $\boldsymbol{f}$ is a map from M to itself and k is an integer index. Note that one could equivalently study continuous-time systems of the form $\dot{\boldsymbol{x}}(t) = \boldsymbol{f}(\boldsymbol{x}(t))$, but here we adopt the discrete-time setting, as we are ultimately interested in analysing discrete-time data. The *Koopman operator* is a linear operator U that acts on scalar-valued functions on M in the following manner: for any scalar-valued function $g : M \to \mathbb{R}$, U maps g into a new function Ug given by

$$Ug(\boldsymbol{x}) = g(\boldsymbol{f}(\boldsymbol{x})). \tag{2.2}$$

Note that U is a linear operator, since $U(\alpha g_1 + \beta g_2)(\boldsymbol{x}) = \alpha Ug_1(\boldsymbol{x}) + \beta Ug_2(\boldsymbol{x})$ for any functions g_1, g_2 and scalars α, β. Although the dynamical system is nonlinear and evolves on a finite-dimensional manifold M, the Koopman operator U is linear, but infinite dimensional.

The idea is to analyse the flow dynamics governed by (2.1) only from available data – collected either numerically or experimentally – using the eigenfunctions and eigenvalues of U. To this end, let $\varphi_j : M \to \mathbb{R}$ denote eigenfunctions and $\lambda_j \in \mathbb{C}$ denote eigenvalues of the Koopman operator,

$$U\varphi_j(\boldsymbol{x}) = \lambda_j \varphi_j(\boldsymbol{x}), \qquad j = 1, 2, \ldots, \tag{2.3}$$

and consider a vector-valued *observable* $\boldsymbol{g} : M \to \mathbb{R}^p$. For instance, if $\boldsymbol{x} \in M$ contains the full information about a flow field at a particular time, $\boldsymbol{g}(\boldsymbol{x})$ is a vector of any quantities of interest, such as a velocity measurements at various points in the flow. If each of the p components of $\boldsymbol{g}$ lies within the span of the eigenfunctions φ_j, then, as in Mezić (2005), we may expand the vector-valued $\boldsymbol{g}$ in terms of these eigenfunctions as

$$\boldsymbol{g}(\boldsymbol{x}) = \sum_{j=1}^{\infty} \varphi_j(\boldsymbol{x}) \boldsymbol{v}_j. \tag{2.4}$$

Here, we have assumed that components of $\boldsymbol{g}$ lie within the span of the eigenfunctions of U. If this is not the case, then to proceed rigorously, one may split U into

regular and singular components, and project components of $\boldsymbol{g}$ onto the span of the eigenfunctions, as done in Mezić (2005).

We typically think of the expression (2.4) as expanding $\boldsymbol{g}(\boldsymbol{x})$ as a linear combination of the vectors $\boldsymbol{v}_j$, but we may alternatively think of this expression as expanding the function $\boldsymbol{g}(\boldsymbol{x})$ as a linear combination of the eigenfunctions φ_j of U, where now $\boldsymbol{v}_j$ are the (vector) coefficients in the expansion. In this paper, we will refer to the eigenfunctions φ_j as *Koopman eigenfunctions*, and the corresponding vectors $\boldsymbol{v}_j$ in (2.4) the *Koopman modes* of the map $\boldsymbol{f}$, corresponding to the observable $\boldsymbol{g}$. Note that iterates of $\boldsymbol{x}_0$ are then given by

$$\boldsymbol{g}(\boldsymbol{x}_k) = \sum_{j=1}^{\infty} U^k \varphi_j(\boldsymbol{x}_0)\boldsymbol{v}_j = \sum_{j=1}^{\infty} \lambda_j^k \varphi_j(\boldsymbol{x}_0)\boldsymbol{v}_j. \tag{2.5}$$

The *Koopman eigenvalues*, $\lambda_j \in \mathbb{C}$, therefore characterize the temporal behaviour of the corresponding Koopman mode $\boldsymbol{v}_j$: the phase of λ_j determines its frequency, and the magnitude determines the growth rate. Note that, as described in Mezić (2005), for a system evolving on an attractor, the Koopman eigenvalues always lie on the unit circle.

The following examples illustrate that eigenvalues and eigenfunctions of the Koopman operator are related to objects we routinely use in fluid mechanics, such as global eigenmodes (for linear systems) and the discrete Fourier transform (for periodic solutions of (2.1)).

2.1. *Example: Koopman modes for linear systems*

Suppose M is an n-dimensional linear space, and suppose the map $\boldsymbol{f}$ is linear, given by

$$\boldsymbol{f}(\boldsymbol{x}) = \boldsymbol{A}\boldsymbol{x}. \tag{2.6}$$

It turns out that eigenvalues of $\boldsymbol{A}$ are also eigenvalues of U, and the eigenvectors of $\boldsymbol{A}$ are related to eigenfunctions of U as well.

Let $\boldsymbol{v}_j$ and λ_j denote eigenvectors and eigenvalues of $\boldsymbol{A}$:

$$\boldsymbol{A}\boldsymbol{v}_j = \lambda_j \boldsymbol{v}_j, \qquad j = 1, \dots, n, \tag{2.7}$$

and let $\boldsymbol{w}_j$ be corresponding eigenfunctions of the adjoint $\boldsymbol{A}^*$ (i.e. $\boldsymbol{A}^*\boldsymbol{w}_j = \bar{\lambda}_j \boldsymbol{w}_j$), normalized so that $\langle \boldsymbol{v}_j, \boldsymbol{w}_k \rangle = \delta_{jk}$, where $\langle \cdot, \cdot \rangle$ denotes an inner product on M. Next, define scalar-valued functions

$$\varphi_j(\boldsymbol{x}) = \langle \boldsymbol{x}, \boldsymbol{w}_j \rangle, \qquad j = 1, \dots, n. \tag{2.8}$$

Then φ_j are eigenfunctions of U, with eigenvalues λ_j, since

$$U\varphi_j(\boldsymbol{x}) = \varphi_j(\boldsymbol{A}\boldsymbol{x}) = \langle \boldsymbol{A}\boldsymbol{x}, \boldsymbol{w}_j \rangle = \langle \boldsymbol{x}, \boldsymbol{A}^*\boldsymbol{w}_j \rangle = \lambda_j \langle \boldsymbol{x}, \boldsymbol{w}_j \rangle = \lambda_j \varphi_j(\boldsymbol{x}). \tag{2.9}$$

(Note that, unlike $\boldsymbol{A}$, the operator U has a countably infinite number of eigenvalues, since λ_j^k is also an eigenvalue, with eigenfunction $\varphi_j(\boldsymbol{x})^k$, for any integer k.) Now, for any $\boldsymbol{x} \in M$, as long as $\boldsymbol{A}$ has a full set of eigenvectors, we may write

$$\boldsymbol{x} = \sum_{j=1}^{n} \langle \boldsymbol{x}, \boldsymbol{w}_j \rangle \boldsymbol{v}_j = \sum_{j=1}^{n} \varphi_j(\boldsymbol{x})\boldsymbol{v}_j. \tag{2.10}$$

For linear systems, then, the Koopman modes coincide with the eigenvectors of $\boldsymbol{A}$.

<center>*2.2. Example: Koopman modes for periodic solutions*</center>

Returning to the nonlinear setting, suppose we have a set of distinct vectors $S = \{\boldsymbol{x}_0, \ldots, \boldsymbol{x}_{m-1}\}$ that form a periodic solution of (2.1), such that $\boldsymbol{x}_{k+m} = \boldsymbol{x}_k$ for all k. A common way to analyse such a solution is to take its discrete Fourier transform, which defines a new set of vectors $\{\hat{\boldsymbol{x}}_0, \ldots, \hat{\boldsymbol{x}}_{m-1}\}$ that satisfy

$$\boldsymbol{x}_k = \sum_{j=0}^{m-1} e^{2\pi i j k/m} \hat{\boldsymbol{x}}_j, \qquad k = 0, \ldots, m-1. \tag{2.11}$$

Now, define a set of functions $\varphi_j : S \to \mathbb{C}$ by

$$\varphi_j(\boldsymbol{x}_k) = e^{2\pi i j k/m}, \qquad j, k = 0, \ldots, m-1. \tag{2.12}$$

Then φ_j are eigenfunctions of the Koopman operator U, with eigenvalues $e^{2\pi i j/m}$, since

$$U\varphi_j(\boldsymbol{x}_k) = \varphi_j(\boldsymbol{f}(\boldsymbol{x}_k)) = \varphi_j(\boldsymbol{x}_{k+1}) = e^{2\pi i j(k+1)/m} = e^{2\pi i j/m}\varphi_j(\boldsymbol{x}_k). \tag{2.13}$$

Therefore, we may write the expansion (2.11) as

$$\boldsymbol{x}_k = \sum_{j=0}^{m-1} \varphi_j(\boldsymbol{x}_k)\hat{\boldsymbol{x}}_j. \tag{2.14}$$

Note the similarity with (2.10). Thus, if we restrict our phase space to the periodic orbit S, the Koopman modes defined as in the previous subsection are the vectors $\hat{\boldsymbol{x}}_j$ given by the discrete Fourier transform, and the phases of the corresponding eigenvalues are the frequencies $2\pi j/m$. This result in fact applies more generally to non-periodic systems, as discussed in Mezić & Banaszuk (2004) and Mezić (2005): when the dynamics are restricted to any attractor, the Koopman modes may be calculated by harmonic averages, which for finite-time datasets reduce to discrete Fourier transforms.

3. Computation of Koopman modes from snapshots

Here, we present an algorithm for computing the Koopman modes defined in the previous section, given only values of a particular observable (snapshots), sampled at regular times. As before, we will assume that the dynamics are governed by (2.1), and that for any state $\boldsymbol{x}$, we can measure a vector-valued observable $\boldsymbol{g}(\boldsymbol{x}) \in \mathbb{R}^p$. For instance, if we have access to a grid of velocity vectors in a limited region of space (e.g. obtained via PIV), then p is the number of grid points times velocity components.

In particular, below we show that the commonly used Arnoldi algorithm, when applied to a nonlinear system, actually produces approximations to eigenvalues of the Koopman operator, and their corresponding modes as defined in the previous section. We first consider linear systems, and present a version of the Arnoldi algorithm that does not require explicit knowledge of the underlying operator $\boldsymbol{A}$. This variant of the algorithm is described by Saad (Saad 1980, p. 287), and is the same as that referred to as dynamic mode decomposition by Schmid & Sesterhenn (2008). We then provide an alternative interpretation of the algorithm that applies to nonlinear systems, and connects with the Koopman modes.

<center>*3.1. Arnoldi algorithm for linear systems*</center>

Assume one has a linear dynamical system

$$\boldsymbol{x}_{k+1} = \boldsymbol{A}\boldsymbol{x}_k, \tag{3.1}$$

where $x_k \in \mathbb{R}^n$, and n is so large that we cannot compute eigenvalues of A directly. A standard method for computing estimates of these eigenvalues is a *Krylov method*, in which one starts with an initial vector x_0 (often chosen to be a random vector), and computes iterates of x_0. After $m - 1$ iterations, one has a collection of m vectors that span a *Krylov subspace*, given by span$\{x_0, Ax_0, \ldots, A^{m-1}x_0\}$. One then finds approximate eigenvalues and eigenvectors by projecting A onto this m-dimensional subspace, and computing eigenvectors and eigenvalues of the resulting low-rank operator. If we stack the data vectors into an $n \times m$ matrix

$$K = [x_0 \quad Ax_0 \quad A^2x_0 \quad \cdots \quad A^{m-1}x_0] \tag{3.2}$$

$$= [x_0 \quad x_1 \quad x_2 \quad \cdots \quad x_{m-1}], \tag{3.3}$$

then we wish to find approximate eigenvectors of A as linear combinations of the columns of K. The *Arnoldi algorithm* is a type of Krylov method in which one orthonormalizes the iterates at each step, and it therefore involves computing the action of A on arbitrary vectors. A variant of this algorithm that does not require explicit knowledge of A is given below.

First, consider the special case where the mth iterate x_m is a linear combination of the previous iterates. Following §2 of Ruhe (1984), we may write

$$x_m = Ax_{m-1} = c_0x_0 + \cdots + c_{m-1}x_{m-1} = Kc, \tag{3.4}$$

where $c = (c_0, \ldots, c_{m-1})$. Thus, we have

$$AK = KC, \tag{3.5}$$

where C is a *companion matrix* given by

$$C = \begin{bmatrix} 0 & 0 & \cdots & 0 & c_0 \\ 1 & 0 & & 0 & c_1 \\ 0 & 1 & & 0 & c_2 \\ \vdots & & \ddots & & \vdots \\ 0 & 0 & \cdots & 1 & c_{m-1} \end{bmatrix}. \tag{3.6}$$

The eigenvalues of C are then a subset of the eigenvalues of A: if

$$Ca = \lambda a,$$

then using (3.5), one verifies that $v = Ka$ is an eigenvector of A, with eigenvalue λ.

More generally, if the mth iterate is not a linear combination of the previous iterates, then instead of the equality (3.4), we have a residual

$$r = x_m - Kc,$$

which is minimized when c is chosen such that r is orthogonal to span$\{x_0, \ldots, x_{m-1}\}$. In this case, the relation (3.5) becomes $AK = KC + re^T$, where $e = (0, \ldots, 1) \in \mathbb{R}^m$. The eigenvalues of C are then approximations to the eigenvalues of A, called *Ritz values*, and the corresponding approximate eigenvectors are given by $v = Ka$, called *Ritz vectors*. Note that the full Arnoldi method is more numerically stable than this method, and reduces A to an upper Hessenberg matrix, rather than a companion matrix.

3.1.1. *Algorithm*

An important feature of the above algorithm is that it does not require explicit knowledge of the matrix A: all it requires is a sequence of vectors, as summarized below.

Consider a sequence $\{x_0, \dots, x_m\}$ where $x_j \subset \mathbb{R}^n$. Define the *empirical Ritz values* λ_j and *empirical Ritz vectors* v_j of this sequence by the following algorithm:

(i) Define K by (3.3) and find constants c_j such that

$$r = x_m - \sum_{j=0}^{m-1} c_j x_j = x_m - Kc, \qquad r \perp \mathrm{span}\{x_0, \dots, x_{m-1}\}. \tag{3.7}$$

(ii) Define the companion matrix C by (3.6) and find its eigenvalues and eigenvectors

$$C = T^{-1} \Lambda T, \qquad \Lambda = \mathrm{diag}(\lambda_1, \dots, \lambda_m), \tag{3.8}$$

where eigenvectors are columns of T^{-1}.

(iii) Define v_j to be the columns of $V = K T^{-1}$.

If $x_j = A^j x_0$, then the empirical Ritz values λ_j are the usual Ritz values of A after m steps of the Arnoldi method, and v_j are the corresponding Ritz vectors. These, then, are (usually) good approximations of the eigenvalues and eigenvectors of A. However, if we do not have $x_j = A^j x_0$ (for instance, if the sequence is generated by a nonlinear map), then at this point, it is not clear what the above algorithm produces. We show below that for a nonlinear system, the algorithm produces approximations of the Koopman modes and associated eigenvalues.

3.2. *Modal decomposition for nonlinear systems*

A more general interpretation of the above algorithm is provided by the following theorem, which will be used below.

THEOREM 1. *Consider a set of data $\{x_0, \dots, x_m\}$, and let λ_j, v_j be the empirical Ritz values and vectors of this sequence. Assume the λ_j are distinct. Then*

$$x_k = \sum_{j=1}^m \lambda_j^k v_j, \qquad k = 0, \dots, m-1, \tag{3.9}$$

$$x_m = \sum_{j=1}^m \lambda_j^m v_j + r, \qquad r \perp \mathrm{span}\{x_0, \dots, x_{m-1}\}. \tag{3.10}$$

Proof. Note that (3.9) may be written in matrix form as

$$K := [x_0 \ x_1 \ \cdots \ x_{m-1}] = [v_1 \ \cdots \ v_m] \begin{bmatrix} 1 & \lambda_1 & \lambda_1^2 & \cdots & \lambda_1^{m-1} \\ 1 & \lambda_2 & \lambda_2^2 & \cdots & \lambda_2^{m-1} \\ \vdots & \vdots & \vdots & \ddots & \vdots \\ 1 & \lambda_m & \lambda_m^2 & \cdots & \lambda_m^{m-1} \end{bmatrix}. \tag{3.11}$$

The rightmost matrix above is a *Vandermonde matrix*, which we will denote $\tilde{T}$. Note that Vandermonde matrices and companion matrices are closely related, in that $\tilde{T}$ diagonalizes the companion matrix C defined in (3.6), as long as the eigenvalues $\lambda_1, \dots, \lambda_m$ are distinct. That is, $\tilde{T}$ is precisely the matrix T in (3.8), and so $K = V\tilde{T}$, which verifies (3.11), and therefore (3.9). Equation (3.10) then follows from the last

column of the equality

$$[\boldsymbol{x}_1 \quad \boldsymbol{x}_2 \quad \cdots \quad \boldsymbol{x}_m] = \boldsymbol{KC} + \boldsymbol{r}\boldsymbol{e}^T = \boldsymbol{K}\tilde{\boldsymbol{T}}^{-1}\boldsymbol{\Lambda}\tilde{\boldsymbol{T}} + \boldsymbol{r}\boldsymbol{e}^T = \boldsymbol{V}\boldsymbol{\Lambda}\tilde{\boldsymbol{T}} + \boldsymbol{r}\boldsymbol{e}^T. \qquad (3.12)$$

To illustrate how this theorem provides a connection with Koopman modes, consider a vector-valued observable $\boldsymbol{g} : M \to \mathbb{R}^p$ for the dynamical system (2.1) and its expansion (2.4) in the Koopman modes. Suppose we have a sequence of observations $\boldsymbol{g}(\boldsymbol{x}_k)$, for $k = 0, \ldots, m$, and let $\tilde{\lambda}_j$ and $\tilde{\boldsymbol{v}}_j$ be the empirical Ritz values and vectors for this sequence. Then, by Theorem 1, we have

$$\boldsymbol{g}(\boldsymbol{x}_k) = \sum_{j=1}^{m} \tilde{\lambda}_j^k \tilde{\boldsymbol{v}}_j, \qquad k = 0, \ldots, m-1, \qquad (3.13)$$

$$\boldsymbol{g}(\boldsymbol{x}_m) = \sum_{j=1}^{m} \tilde{\lambda}_j^m \tilde{\boldsymbol{v}}_j + \boldsymbol{r}, \qquad (3.14)$$

with $\boldsymbol{r} \perp \text{span}\{\boldsymbol{g}(\boldsymbol{x}_0), \ldots, \boldsymbol{g}(\boldsymbol{x}_{m-1})\}$. Comparing with the expansion (2.5), the empirical Ritz values $\tilde{\lambda}_j$ and vectors $\tilde{\boldsymbol{v}}_j$ behave in precisely the same manner as the eigenvalues λ_j and modes $\boldsymbol{v}_j$ of U, but for the finite sum in (3.13) instead of the infinite sum (2.5).

If $\boldsymbol{r} = \boldsymbol{0}$ in (3.14), then as far as the data is concerned, the approximate modes are indistinguishable from 'true' eigenvalues and Koopman modes of U, with the expansion (2.4) consisting only of a finite number of terms.

If $\boldsymbol{r} \neq \boldsymbol{0}$, then there is some error, but this is in a sense the best one can do, since the $m + 1$ observations cannot in general be spanned by m modes. In fact, by the projection theorem, the error $\boldsymbol{r}$ in (3.14) is the same as the smallest possible error in projecting $\boldsymbol{g}(\boldsymbol{x}_m)$ onto any modes $\tilde{\boldsymbol{v}}_j$ formed from linear combinations of the first m data vectors. In this sense, the values $\tilde{\lambda}_j$ are then approximations of true eigenvalues λ_j of U, and the vectors $\tilde{\boldsymbol{v}}_j$ are approximations of the Koopman modes $\boldsymbol{v}_j$, scaled by the constant values $\varphi_j(\boldsymbol{x}_0)$.

Note that an interesting situation occurs if $\boldsymbol{g}(\boldsymbol{x}_0) = \boldsymbol{g}(\boldsymbol{x}_m)$. Then in (3.7), $c_0 = 1$ and $c_j = 0$ for all other values of j. The empirical Ritz values are then the mth roots of unity, $\lambda_j = \mathrm{e}^{2\pi \mathrm{i} j/m}$, and the Vandermonde matrix $\boldsymbol{T}$ is the discrete Fourier transform matrix. Thus, in this case, the empirical Ritz vectors are given by the discrete Fourier transform of the data, at frequencies $2\pi j/m$, as illustrated by the example in §2.2.

4. Example: jet in crossflow

The jet-in-crossflow configuration appears in a variety of applications and is a common way of mixing a jet fluid – injected through an orifice – with a uniform crossflow. Recently, Bagheri *et al.* (2009*b*) showed that the jet in crossflow exhibits self-sustained global oscillations that can be associated with vortex shedding in different spatial regions. Using time traces, we extract and quantify here the oscillatory behaviour of the flow from fully nonlinear direct numerical simulations (DNS) and show that the computed Koopman modes identify the relevant frequencies and the corresponding three-dimensional flow structures automatically.

The parameters and the numerical code are the same as in the DNS performed in Bagheri *et al.* (2009*b*); the jet inflow ratio is $R \equiv V_{jet}/U_\infty = 3$, the Reynolds number is $Re_{\delta_0^*} \equiv U_\infty \delta_0^*/\nu = 165$ and the ratio between the crossflow displacement thickness and the jet diameter is $\delta_0^*/D = 1/3$. The incompressible Navier–Stokes equations over a flat plate are solved using a Fourier–Chebyshev spectral method (Chevalier *et al.* 2007) and the jet with an initially parabolic velocity profile is introduced as an
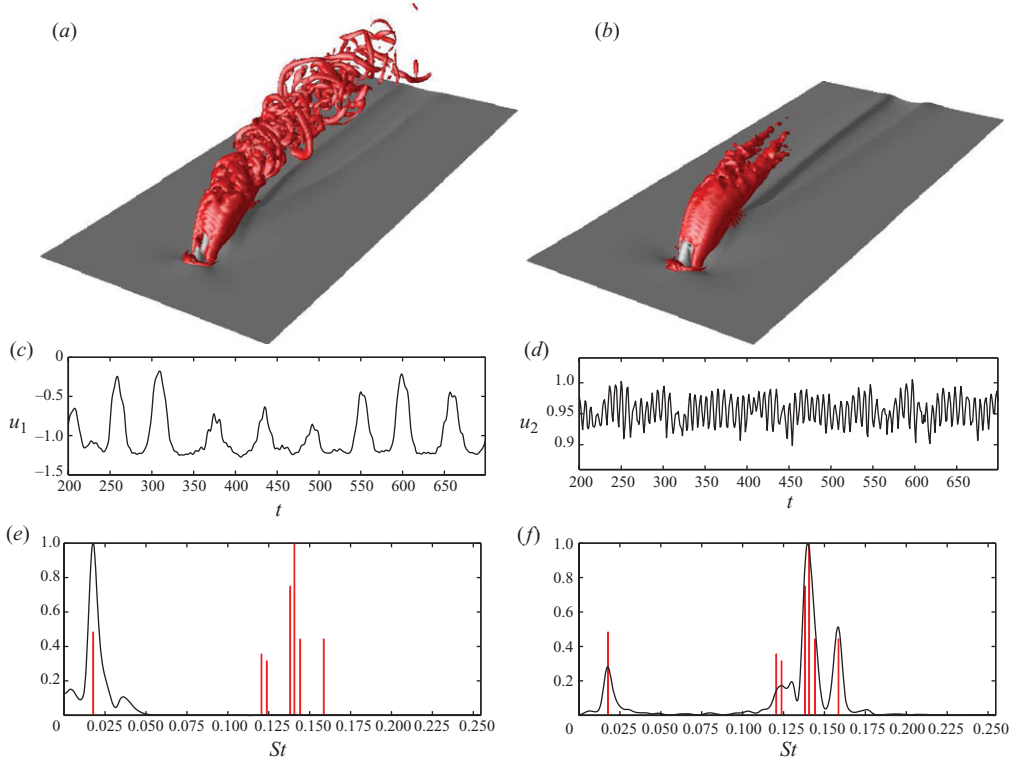
FIGURE 1. (a) Snapshot of the flow field at $t = 400$. Red and grey isocontours represent $\lambda_2 = -0.1$ and $u = 0.2$ (near the wall) respectively. (b) The same quantities for the time-averaged flow which also is the first Koopman mode. (c, d) Time signal probes located near the wall and on the jet shear layer respectively (see the text). (e, f) The spectral content of the corresponding time signals in (c) and (d) are shown in black and the magnitudes of the first seven pairs of Koopman modes at each frequency are shown in red. The amplitudes are normalized with their maximum values.

inhomogeneous boundary condition for the wall-normal velocity component at the wall ($y = 0$). The grid resolution is $256 \times 201 \times 144$ grid points in a computational box $(L_x, L_y, L_z) = (75, 20, 30)\delta_0^*$. The three-dimensional flow behaviour is triggered by an asymmetric localized perturbation imposed at $t = 0$. For the exact form of the jet-profile and further numerical details see Bagheri *et al.* (2009b).

The flow physics of the jet-in-crossflow has been studied extensively (see e.g. Fric & Roshko 1994; Kelso, Lim & Perry 1996; Muppidi & Mahesh 2007) and it is shown that it is mainly characterized by four to five vortical structures depending on R and Re. In the present study, we could identify two steady, two unsteady and one quasi-steady vortex systems. Four of these can be seen in figure 1(a, b) where isocontours of the λ_2 criterion (red) (Jeong & Hussain 1995) and the streamwise velocity (grey) are displayed. The most significant unsteady feature of the jet is the highly unsteady shear-layer vortices (see figure 1a): These half-ringed shaped vortices grow along the jet trajectory, lead to a breakdown of the ordered flow and, eventually, dissipate due to viscous effects. Connected to the shear layer are the vertically oriented 'upright vortices', which are periodically appearing vortices connecting the jet body and the wall layer in the wake of the jet. These structures are easily identified from the vorticity field, but are not visible here. On the other hand, the steady counter-rotating vortex
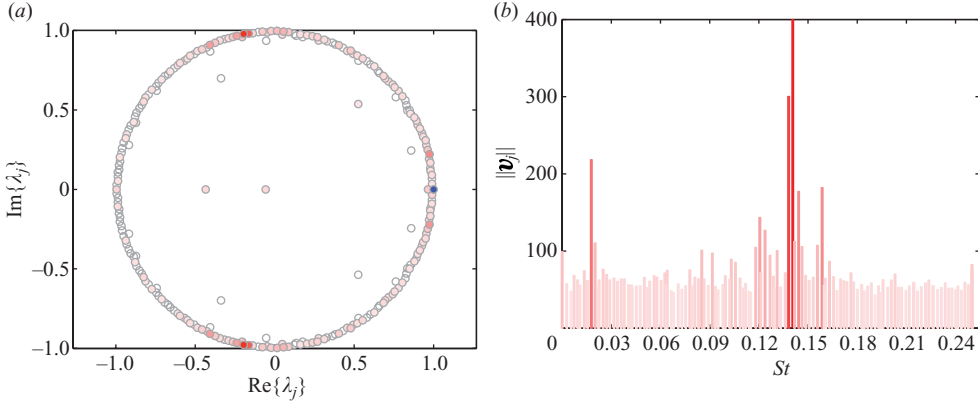
FIGURE 2. (a) The empirical Ritz values λ_j. The value corresponding to the first Koopman mode is shown with the blue symbol. (b) The magnitudes of the Koopman modes (except the first one) at each frequency. In both figures, the colours vary smoothly from red to white, depending on the magnitude of the corresponding mode.

pair (CVP), characteristic of the jet trajectory, is visible in the time-averaged mean flow (figure 1b). Similarly visible in the mean, the horse-shoe vortices wrap around the column of jet very close to the wall and, further downstream, lead to the appearance of the quasi-steady wall-vortex system as shown by the distortion of the velocity isocontour in figure 1(a, b). These essentially streamwise-oriented vortices are subject to low-frequency oscillations of the wall-vortex system originating in a shedding of the separation zone just downstream of the jet orifice, and induce a movement of the whole jet body. The steady structures were also identified in the steady nonlinear Navier–Stokes solution computed numerically by Bagheri *et al.* (2009b).

As found in Bagheri *et al.* (2009b), two distinct self-sustained oscillations could be detected from the DNS. A high-frequency shedding of the shear-layer vortices and a very low frequency shedding of the wall vortices. Figure 1(c) shows the time signal of the streamwise velocity $u^1(\boldsymbol{x}_P^1, t)$ from a probe located just downstream of the jet orifice and close the wall, $\boldsymbol{x}_P^1 = (x, y, z) = (10.7, 1, 0)$. In figure 1(e) its corresponding power spectrum shows the frequency content $\hat{u}^1(\omega)$ of $u^1(t)$. The peak frequency corresponds to a vortex shedding of wake vortices with the Strouhal number $St \equiv f D / V_{jet} = 0.0174$.

In figure 1(d, f), a second probe located a few jet diameters along the jet trajectory $\boldsymbol{x}_P^2 = (12, 6, 2)$, shows a second oscillation that can be identified with the shedding of the shear-layer vortices. The peak frequency oscillates with $St = 0.141$ which is nearly one order of magnitude larger than the low-frequency mode. Note that the peak frequencies of the power spectra vary slightly depending on the location of the probe.

4.1. *Koopman modes and frequencies*

In this section we compute the Koopman modes and show that they directly allow an identification of the various shedding frequencies. The empirical Ritz values λ_j and the empirical vectors $\boldsymbol{v}_j$ of a sequence of flow fields $\{\boldsymbol{u}_0, \boldsymbol{u}_1, \ldots, \boldsymbol{u}_{m-1}\} = \{\boldsymbol{u}(t=200), \boldsymbol{u}(t=202), \ldots, \boldsymbol{u}(t=700)\}$ with $m = 251$ are computed using the algorithm described earlier. Thus, the transient time ($t < 200$) is not sampled and only the asymptotic motion in phase space is considered.

Figure 2(a) shows that nearly all the Ritz values are on the unit circle $|\lambda_j| = 1$ indicating that the sample points $\boldsymbol{u}_i$ lie on or near an attracting set. The Koopman eigenvalue corresponding to the first Koopman mode is the time-averaged flow and

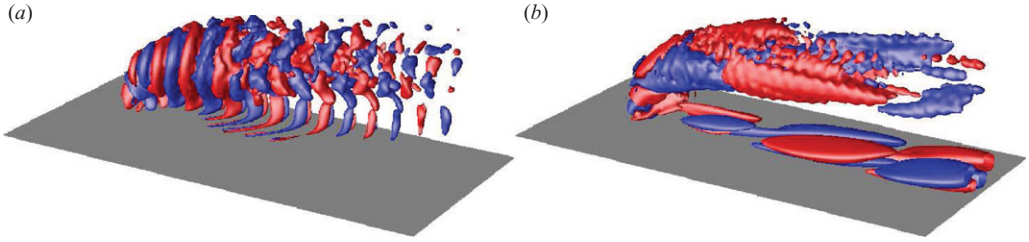(a)   (b)

FIGURE 3. Positive (red) and negative (blue) contour levels of the streamwise velocity components of two Koopman modes. The wall is shown in grey. (a) Mode 2, with $\|v_2\| = 400$ and $St_2 = 0.141$. (b) Mode 6, with $\|v_6\| = 218$ and $St_6 = 0.0175$.

is depicted with blue symbol in figure 2(a). This mode, shown in figure 1(b), captures the steady flow structures as discussed previously. In figure 2(a), the other (unsteady) Ritz values vary smoothly in colour from red to white, depending on the magnitude of the corresponding Koopman mode. The magnitudes defined by the global energy norm $\|v_j\|$, and are shown in figure 2(b) with the same colouring as the spectrum. In figure 2(b) each mode is displayed with a vertical line scaled with its magnitude at its corresponding frequency $\omega_j = \mathrm{Im}\{\log(\lambda_j)\}/\Delta t$ (with $\Delta t = 2$ in our case). Only the $\omega_j \geqslant 0$ are shown, since the eigenvalues come in complex conjugate pairs. Ordering the modes with respect to their magnitude, the first (2–3) and second (4–5) pair of modes oscillate with $St_2 = 0.141$ and $St_4 = 0.136$ respectively, whereas the third pair of modes (6–7) oscillate with $St_6 = 0.017$. All linear combinations of the frequencies excite higher modes, for instance, the nonlinear interaction of the first and third pair results in the fourth pair, i.e. $St_8 = 0.157$ and so on.

In figures 1(e) and 1(f) the power spectra of the two DNS time signals (black lines) are compared to the frequencies obtained directly from the Ritz eigenvalues (red vertical lines). The shedding frequencies and a number of higher harmonics are in very good agreement with the frequencies of the Koopman modes. In particular, the dominant Koopman eigenvalues match the frequencies for the wall mode ($St = 0.017$) and the shear-layer mode ($St = 0.14$). Note that the probe signals are local measures of the frequencies at one spatial point, whereas the Koopman eigenvalues correspond to global modes in the flow with time-periodic motion.

The streamwise velocity component u of Koopman modes 2 and 6 are shown in figure 3. Each mode represents a flow structure that oscillates with one single frequency, and the superposition of several of these modes results in the quasi-periodic global system. The high-frequency mode 2 (figure 3a) can be associated with the shear layer vortices; along the jet trajectory there is first a formation of ring-like vortices that eventually dissolve into smaller scales due to viscous dissipation. Also visible are upright vortices: on the leeward side of the jet, there is a significant structure extending towards the wall. This indicates that the shear-layer vortices and the upright vortices are coupled and oscillate with the same frequency. The spatial structures of modes 4 and 8 are very similar to those of mode 2, as one expects, since the frequencies are very close.

On the other hand, the low-frequency mode 6 shown in figure 3(b) features large-scale positive and negative streamwise velocity near the wall, which can be associated with shedding of the wall vortices. However, this mode also has structures along the jet trajectory further away from the wall. This indicates that the shedding of wall vortices is coupled to the jet body, i.e. the low frequency can be detected nearly anywhere in the vicinity of the jet since the whole jet is oscillating with that frequency.

Mode	DNS	Global	POD	Koopman
Shear layer	0.141	0.169	0.138, 0.158, 0.121	0.141
Wall	0.017	0.043	0.0188, 0.0094, 0.158, 0.121	0.017

TABLE 1. Comparison of the frequencies ($St = fD/V_{jet}$) obtained from DNS probes (shown in figure 1); the global eigenmodes of the linearized Navier–Stokes; POD modes 1 and 6, corresponding to mainly shear-layer and wall oscillations, respectively; and Koopman modes.
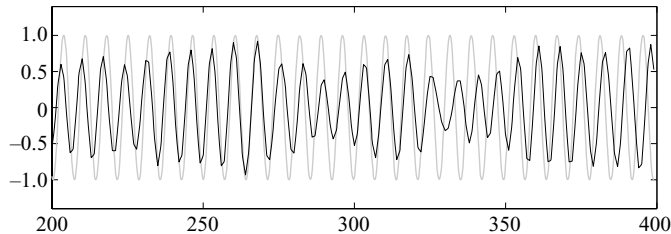

FIGURE 4. Comparison of time coefficients: the projection of the flow field onto the most energetic POD mode (black), and the coefficient of the most energetic Koopman mode (grey).

4.2. *Comparison with linear global modes and POD modes*

The linear global eigenmodes of the Navier–Stokes equations linearized about an unstable steady state solution were computed by Bagheri *et al.* (2009*b*) for the same flow parameters as the current study. They computed 22 complex–conjugate unstable modes using the Arnoldi method combined with a time-stepper approach. The frequency of the most unstable (antisymmetric) mode associated with the shear-layer instability was $St = 0.169$, not far from the value $St = 0.14$ observed for the DNS. However, the mode with the lowest frequency associated with the wall vortices was $St = 0.043$, far from the observed frequency of $St = 0.017$. These frequencies are summarized in table 1. The global eigenmodes capture the dynamics only in a neighbourhood of the unstable fixed point, while the Koopman modes correctly capture the behaviour on the attractor.

We also compared the Koopman modes with modes determined by POD of the same dataset. The POD modes themselves are shown in Bagheri, Schlatter & Henningson (2009*a*) and capture similar spatial structures to the Koopman modes shown in figure 3. The most striking distinction is in the time coefficients, an example of which is shown in figure 4: while a single Koopman mode contains, by construction, only a single frequency component, the POD modes capture the most energetic structures, resulting in modes that contains several frequencies. The coefficient of the first POD mode oscillates mainly with frequency $St = 0.138$, which is close to the shear-layer oscillation frequency $St = 0.141$ observed in DNS. However, the signal contains other frequencies as well, resulting from the interaction of the two fundamental oscillations (shear-layer and wall), $St = 0.138 \pm 0.017$, which cause the beating shown in figure 4. The frequencies present in this most energetic POD mode are also summarized in table 1. Higher POD modes (in this case the sixth) capture the wall oscillations, but the signal is polluted with other frequencies as well. For situations such as the jet in crossflow where one is interested in studying the dynamics of low-frequency oscillations (such as wall modes) separate from high-frequency oscillations (such as

shear-layer modes), the Koopman modes are thus more effective at decoupling and isolating these dynamics.

5. Conclusions

We have presented a method for studying the dynamical behaviour of nonlinear systems, and illustrated the method on a jet in crossflow. The method involves spectral analysis of the Koopman operator, an infinite-dimensional linear operator defined for any nonlinear dynamical system. In particular, given a particular observable (e.g. available measurements from an experiment or simulation), we have defined a set of *Koopman modes* associated with this observable, related to eigenfunctions of the Koopman operator. For the special case of linear systems where the observable is the full flow state, these modes reduce to the global eigenmodes, and for periodic systems, the modes can be determined by the discrete temporal Fourier transform. For more general systems, we have shown that these modes may be computed using a familiar Arnoldi algorithm, applied to samples of the nonlinear system.

We have used these modes to study the dynamical behaviour of a jet in crossflow. The resulting modes illustrate the different spatial structures associated with the shear layer and the near-wall region. For this example, the Koopman modes capture the relevant frequencies more accurately than global eigenmodes of the linearized dynamics, and decouple the different frequency components more effectively than modes determined by POD.

REFERENCES

BAGHERI, S., SCHLATTER, P. & HENNINGSON, D. S. 2009*a* Self-sustained global oscillations in a jet in crossflow. *Theor. Comput. Fluid Dyn.* Manuscript submitted for publication.

BAGHERI, S., SCHLATTER, P., SCHMID, P. J. & HENNINGSON, D. S. 2009*b* Global stability of a jet in crossflow. *J. Fluid Mech.* **624**, 33–44.

CHEVALIER, M., SCHLATTER, P., LUNDBLADH, A. & HENNINGSON, D. S. 2007 A pseudo spectral solver for incompressible boundary layer flows. *Tech. Rep., Trita-Mek* 7.

FRIC, T. F. & ROSHKO, A. 1994 Vortical structure in the wake of a transverse jet. *J. Fluid Mech.* **279**, 1–47.

HOLMES, P., LUMLEY, J. L. & BERKOOZ, G. 1996 *Turbulence, Coherent Structures, Dynamical Systems and Symmetry*. Cambridge University Press.

JEONG, J. & HUSSAIN, F. 1995 On the identification of a vortex. *J. Fluid Mech.* **285**, 69–94.

KELSO, R. M., LIM, T. T. & PERRY, A. E. 1996 An experimental study of round jets in crossflow. *J. Fluid Mech.* **306**, 111–144.

MEZIĆ, I. 2005 Spectral properties of dynamical systems, model reduction and decompositions. *Nonlinear Dyn.* **41**, 309–325.

MEZIĆ, I. & BANASZUK, A. 2004 Comparison of systems with complex behaviour. *Physica* D **197**, 101–133.

MUPPIDI, S. & MAHESH, K. 2007 Direct numerical simulation of round turbulent jets in crossflow. *J. Fluid Mech.* **574**, 59–84.

NOACK, B. R., AFANASIEV, K., MORZYŃSKI, M., TADMOR, G. & THIELE, F. 2003 A hierarchy of low-dimensional models for the transient and post-transient cylinder wake. *J. Fluid Mech.* **497**, 335–363.

Rowley, C. W. 2005 Model reduction for fluids using balanced proper orthogonal decomposition. *Intl J. Bifurcation Chaos* **15** (3), 997–1013.

Ruhe, A. 1984 Rational Krylov sequence methods for eigenvalue computation. *Linear Algebr. Appl.* **58**, 391–405.

Saad, Y. 1980 Variations on Arnoldi's method for computing eigenelements of large unsymmetric matrices. *Linear Algebr. Appl.* **34**, 269–295.

Schmid, P. & Sesterhenn, J. 2008 Dynamic mode decomposition of numerical and experimental data. In *Sixty-First Annual Meeting of the APS Division of Fluid Dynamics*. San Antonio, Texas, USA.